

LETTERS

Optomechanical crystals

Matt Eichenfield¹, Jasper Chan¹, Ryan M. Camacho¹, Kerry J. Vahala¹ & Oskar Painter¹

Periodicity in materials yields interesting and useful phenomena. Applied to the propagation of light, periodicity gives rise to photonic crystals¹, which can be precisely engineered for such applications as guiding and dispersing optical beams^{2,3}, tightly confining and trapping light resonantly⁴, and enhancing nonlinear optical interactions⁵. Photonic crystals can also be formed into planar lightwave circuits for the integration of optical and electrical microsystems⁶. In a photonic crystal, the periodicity of the host medium is used to manipulate the properties of light, whereas a phononic crystal uses periodicity to manipulate mechanical vibrations^{7–13}. As has been demonstrated in studies of Raman-like scattering in epitaxially grown vertical cavity structures¹⁴ and photonic crystal fibres¹⁵, the simultaneous confinement of mechanical and optical modes in periodic structures can lead to greatly enhanced light–matter interactions. A logical next step is thus to create planar circuits that act as both photonic and phononic crystals¹⁶: optomechanical crystals. Here we describe the design, fabrication and characterization of a planar, silicon-chip-based optomechanical crystal capable of co-localizing and strongly coupling 200-terahertz photons and 2-gigahertz phonons. These planar optomechanical crystals bring the powerful techniques of optics and photonic crystals to bear on phononic crystals, providing exquisitely sensitive (near quantum-limited), optical measurements of mechanical vibrations, while simultaneously providing strong nonlinear interactions for optics in a large and technologically relevant range of frequencies.

Many of the salient features of three-dimensional photonic crystal or photonic bandgap materials can be realized in lower-dimensional, planar waveguiding structures with the use of standard lithographic and etching procedures⁶. Here we study both the optical and mechanical properties of a textured silicon-on-insulator microchip, with the aim of demonstrating that photonic crystal structures can also be used to detect, generate, and control mechanical vibrations (phonons) within the same planar, chip-scale architecture.

The geometry of the optomechanical crystal structure considered here is shown in Fig. 1a. The effectively one-dimensional structure consists of a silicon nanobeam (thickness t not shown) with rectangular holes formed by thin cross-bars connected on both sides to thin rails. Figure 1b shows a finite-element-method (FEM) simulation of the optical band structure of such a periodically patterned nanobeam projection (we refer here to the infinitely periodic structure as a projection). The electric field profile for modes at the band edge ($k_x = \pi/A$, the boundary of the first Brillouin zone) are shown to the right of the band structure. The finite structure terminates at its supports on both ends, forming a doubly clamped beam. To form localized resonances in the centre of the structure, the discrete translational symmetry of the patterned beam is intentionally disrupted by a ‘defect’ consisting of a quadratic decrease in the lattice constant A , symmetric about the centre of the beam. The defect forms an effective potential for optical modes at the band edges, with the spatial dependence of the effective potential closely following the spatial properties of the defect¹⁷ (see Fig. 1b inset). Thus the optical modes of the infinitely periodic structure are confined

by a quasi-harmonic potential. This effective potential localizes a ‘ladder’ of modes with Hermite–Gauss envelopes, analogous to the modes of the one-dimensional harmonic potential of quantum mechanics. The localized optical modes of the finite structure (hereafter referred to as Device 1) are also found by FEM simulation and shown in Fig. 1b to the right of the corresponding mode of the projection.

Analogously, Fig. 1c shows a FEM simulation of the mechanical band structure of the infinitely periodic nanobeam. Mechanical modes at the band edge experience an effective potential analogous to the optical modes, localizing certain types of vibrations to the defect region. Owing to symmetry (see Supplementary Information), only the coloured bands give rise to mechanical modes that, when localized by the defect, yield ladders of modes with strong dispersive coupling to the localized optical modes. We classify these optomechanically coupled mechanical modes, from lowest to highest frequency, as the ‘pinch’, ‘accordion’ and ‘breathing’ modes. Exemplary localized mechanical modes for each highlighted band are shown to the right of the corresponding mode of the projection.

The two kinds of waves, mechanical and optical, are on equal footing in this structure. Each mechanical mode has a frequency ν_m and displacement profile $\mathbf{Q}(\mathbf{r})$; each optical mode has a frequency ν_o and electric field profile $\mathbf{E}(\mathbf{r})$, where \mathbf{r} is the position vector. Just as the optical mode volume, $V_o = \int dV (\sqrt{\epsilon} |\mathbf{E}| / \max(|\sqrt{\epsilon} \mathbf{E}|))^2$, describes the electromagnetic localization of the optical mode within a material of dielectric constant $\epsilon(\mathbf{r})$, the mechanical mode volume, $V_m \equiv \int dV (|\mathbf{Q}| / \max(|\mathbf{Q}|))^2$ (see Supplementary Information), describes the effective localization of the mechanical mode within a material of constant mass density and elastic moduli. For both the localized optical and mechanical modes of the patterned beam cavity, the effective mode volume is less than a cubic wavelength. The effective motional mass, being proportional to the mode volume ($m_{\text{eff}} \equiv \rho V_m$; with silicon mass density $\rho_{\text{Si}} = 2.33 \text{ g cm}^{-3}$), is between 50 femtograms (fg) and 1,000 fg for the mechanical modes shown in Fig. 1c.

Drawing on recent work in the field of cavity optomechanics^{18,19}, we describe the coupling between optical and mechanical degrees of freedom (to lowest order) by an effective coupling length $L_{\text{OM}} \equiv \left(\frac{1}{\nu_o} \frac{d\nu_o}{d\alpha} \right)^{-1}$, where the dispersion $d\nu_o/d\alpha$ is the rate of change in the frequency of an optical resonance caused by the mechanical displacement parameterized by α . For this work, α is defined as the maximum displacement of the mechanical mode pattern. By definition then, the smaller L_{OM} , the larger the optical response for a given mechanical displacement. L_{OM} is also the length over which a photon’s momentum is transferred into the mechanical mode as it propagates within the structure, and thus is inversely proportional to the force per photon applied to the mechanical system.

To calculate L_{OM} , we used a perturbative theory of Maxwell’s equations with respect to shifting material boundaries²⁰. The derivative $d\nu_o/d\alpha$ around some nominal position, where the optical fields are known, can be calculated exactly without actually deforming the structure for a surface-normal displacement of the boundaries,

¹Thomas J. Watson Sr Laboratory of Applied Physics, California Institute of Technology, Pasadena, California 91125, USA.

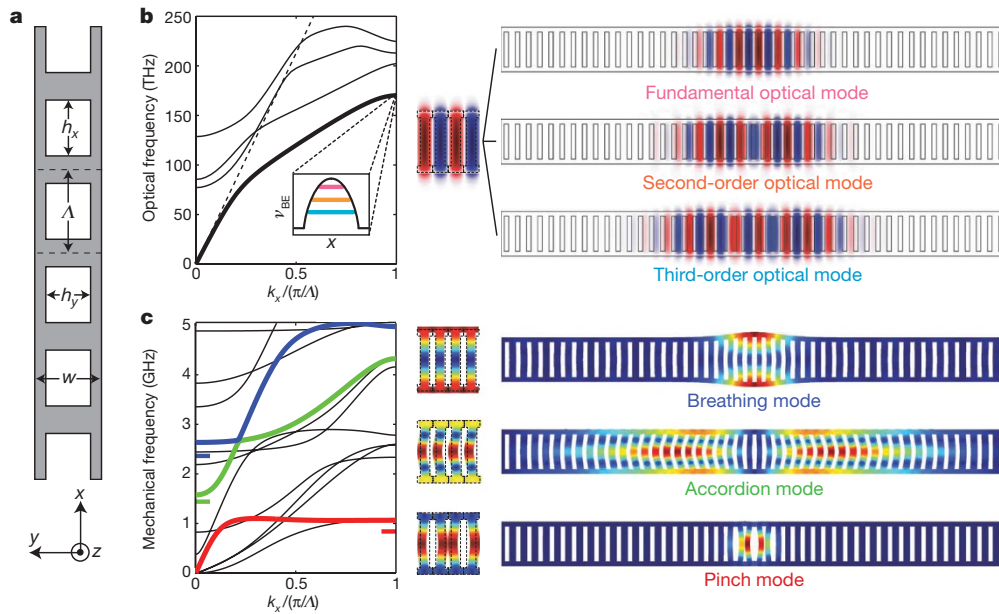


Figure 1 | Optomechanical crystal design. **a**, Geometry of nanobeam structure. **b**, **c**, Optical (**b**) and mechanical (**c**) bands and modes calculated via FEM for the experimentally fabricated (Device 1) silicon nanobeam ($A = 362$ nm, $w = 1,396$ nm, $h_y = 992$ nm, $h_x = 190$ nm, and $t = 220$ nm; isotropic Young's modulus of 168.5 GPa; refractive index $n = 3.493$). The band diagrams and unit-cell modes are calculated for the infinitely periodic beam structure with the above parameters. The coloured bands in panel **c** correspond to optically coupled mechanical modes. The frequency of the fundamental localized mode for each coloured mechanical band is indicated

$h(\alpha; \mathbf{r}) \equiv \mathbf{Q}(\mathbf{r}) \cdot \hat{\mathbf{n}} = \alpha \mathbf{q}(\mathbf{r}) \cdot \hat{\mathbf{n}}$, where $\mathbf{q}(\mathbf{r}) = \mathbf{Q}(\mathbf{r})/\alpha = d\mathbf{Q}(\mathbf{r})/d\alpha$ is the unitless displacement profile of the mechanical mode, and α parameterizes the amplitude of the displacement. Using this perturbative formulation of Maxwell's equations, we find:

$$\frac{1}{L_{\text{OM}}} = \frac{1}{2} \frac{\int dA \left(\frac{d\mathbf{Q}}{d\alpha} \cdot \hat{\mathbf{n}} \right) \left[\Delta \varepsilon |\mathbf{E}_{\parallel}|^2 - \Delta(\varepsilon^{-1}) |\mathbf{D}_{\perp}|^2 \right]}{\int dV \varepsilon |\mathbf{E}|^2} \quad (1)$$

where $\hat{\mathbf{n}}$ is the unit normal vector on the surface of the unperturbed cavity, $\mathbf{D}(\mathbf{r}) = \varepsilon(\mathbf{r})\mathbf{E}(\mathbf{r})$, $\Delta \varepsilon = \varepsilon_1 - \varepsilon_2$, $\Delta(\varepsilon^{-1}) = \varepsilon_1^{-1} - \varepsilon_2^{-1}$, ε_1 is the dielectric constant of the periodic structure, and ε_2 is the dielectric constant of the surrounding medium ($\varepsilon_2 = \varepsilon_0$ in this case). This method of calculating the coupling provides a wealth of intuition about the nature of the coupling and can be used to engineer the structure for strong optomechanical coupling.

Figure 2a and b shows scanning electron microscope images of a fabricated silicon nanobeam with the parameters of Device 1. The optical modes of the nanobeam are probed with a tapered and dimpled optical fibre²¹ in the near-field of the defect cavity, simultaneously sourcing the cavity field and collecting the transmitted light in a single channel (see Methods). Figure 2c shows the low-pass filtered optical transmission spectrum of Device 1 at low optical input power (~ 30 μ W). The optical cavity resonances are identified by comparison to FEM modelling of the optical modes of the structure. The radio frequency (r.f.) spectrum provides information about the optically coupled mechanical modes of the structure through the phase and amplitude modulation imparted to the transmitted light via the mechanical motion of these modes. Figure 2d–g shows the measured photodetector r.f. power spectral density of the optical transmission through the second-order optical cavity resonance (this mode was used because of its deep on-resonance coupling). A series of lower-frequency modes can be seen in the r.f. spectra (~ 200 MHz and higher harmonics), corresponding to compression modes of the entire beam, followed by groups of localized phononic modes of the lattice at 850 MHz (pinch), 1.41 GHz (accordion), and 2.25 GHz

by a horizontal bar of the same colour. The localized modes are calculated for a finite, patterned beam with a central defect (the inset in panel **b** shows the approximate shape of the optical band-edge frequency ν_{BE} versus position x along the length of the beam due to the defect). The defect region consists of $N_{\text{defect}} = 15$ central holes in which the hole-to-hole spacing is varied quadratically from the nominal lattice constant at the beam perimeter (362 nm) to 85% of that value for the two holes straddling the central cross-bar. The total number of holes in the finite beam structure is $N_{\text{total}} = 75$.

(breathing). The transduced signal at low optical power corresponds to thermally excited motion of the mechanical modes, and is inversely proportional to $m_{\text{eff}} L_{\text{OM}}^2$ (see below). At higher optical input power (shown in Fig. 2h), regenerative mechanical oscillation²² of the fundamental breathing mode is excited owing to the strong dynamical back-action¹⁸ between the co-localized phonon and photon modes.

The scaling of frequency with the geometry of the observed vibrational modes can be used to differentiate the various types of modes that are coupled to the optical field. The top panel of Fig. 3a, for instance, shows the trend in frequency of the lowest-frequency mechanical mode of the manifold of modes around 2.3 GHz for a series of devices for which the in-plane geometry has been uniformly scaled. Identified as the fundamental breathing mode in Fig. 2g, the frequency of this mode scales nearly perfectly with the planar geometric scale factor, as expected for the predominantly in-plane vibrations of a thin beam structure. This should be contrasted with the optical modes (Fig. 3a, bottom panel), whose frequencies do not scale simply with the planar geometry, a result of the coupling of in-plane and vertical optical mode confinement. Figure 3b shows the result of a non-uniform in-plane scaling of the optomechanical crystal geometry. The r.f. power spectral density for Device 1 is plotted along with that of a second device, Device 2, which has a lattice constant, $A = 365$ nm, and total length, L , that are essentially identical to those of Device 1, but has a considerably smaller width ($w = 864$ nm, $h_y = 575$ nm, $h_x = 183$ nm). Simulations show that the pinch modes are the lowest-frequency group of localized and optically coupled mechanical modes in both structures (see right panels of Fig. 3b). From the calculated band structures, the ratio of the frequency of the localized pinch-mode manifold, after accounting for the defect, is 1.826 GHz/ 846 MHz = 2.16 for the two devices. Experimentally, the ratio of the fundamental pinch mode frequencies (highlighted in red) is 1.749 GHz/ 805 MHz = 2.17 . This should be compared with the second-order compression mode of the nanobeam, highlighted in yellow in Fig. 3b, which is the lowest-frequency mechanical mode

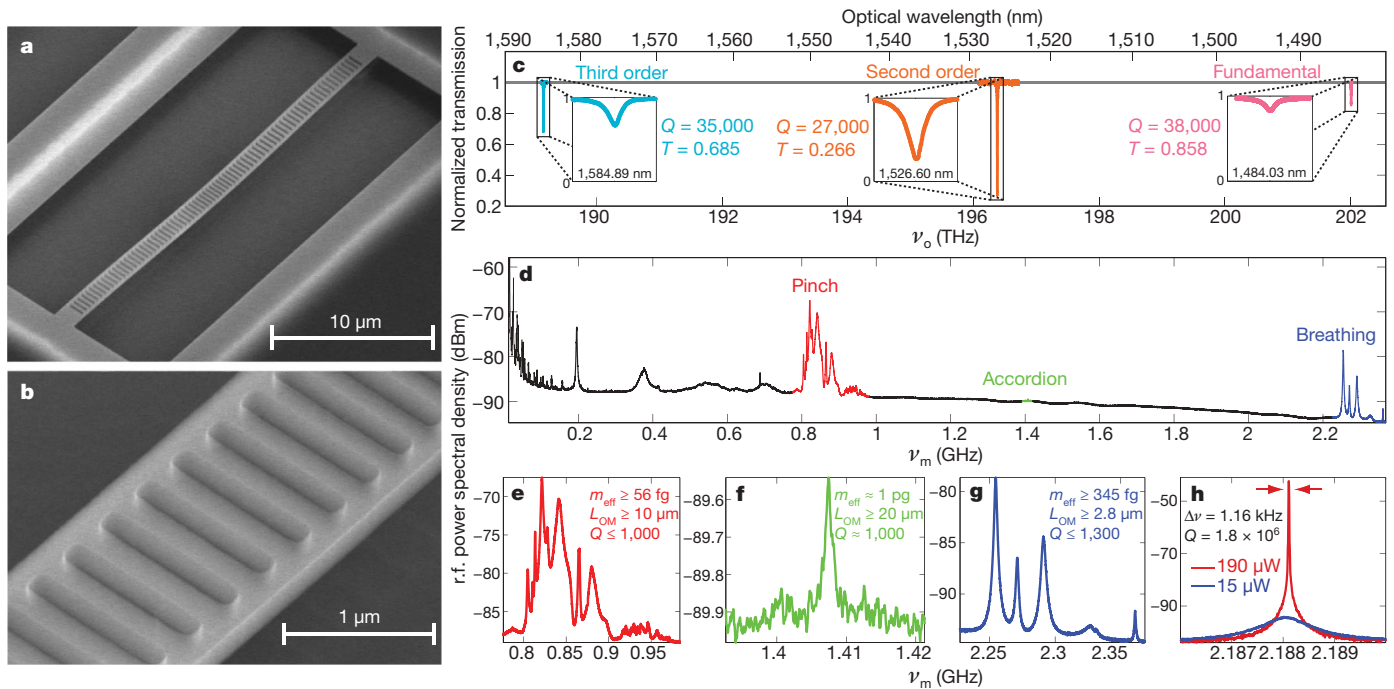


Figure 2 | Photonic and phononic crystal mode spectroscopy. **a, b**, Scanning electron microscope images of the fabricated silicon nanobeam optomechanical crystal. **c**, Optical spectroscopy of Device 1 with the taper waveguide in contact. The taper-loaded quality factor Q and on-resonance normalized transmission level T are indicated for each optical mode. **d**, Mechanical spectroscopy of Device 1 with taper waveguide in contact.

of the global beam structure with optomechanical coupling. This mode has a frequency that should be $\frac{3\pi}{2L} \sqrt{\frac{E}{\langle \rho \rangle}}$, where E is Young's modulus and $\langle \rho \rangle$ is the average linear mass density. The frequency of this mode is measured to be 234 MHz/195 MHz = 1.20 times higher in Device 2 than in Device 1, which is in good agreement with the ratio $\sqrt{\langle \rho_1 \rangle / \langle \rho_2 \rangle} = 1.23$. The difference between the change in the frequencies of the lattice-localized versus beam modes illustrates the independence of these two 'systems'; once the wavelength of the global beam modes approaches the scale of the lattice periodicity, the vibrations become localized and behave independently of the global beam structure (such as the end clamps).

Further details of the properties of the lattice-localized phononic cavity modes can be determined through quantitative study of their optical transduction. Figure 3c shows the r.f. optical transmission spectrum (blue) and fit (black) due to Brownian motion of the breathing modes of Device 1 (that is, at low optical input power), for the three optical modes shown in Figs 1c and 2c. Because the various optical modes have different spatial profiles, each mechanical mode has a different L_{OM} for each optical mode. The root-mean-square (r.m.s.) mechanical amplitude of a mode due to Brownian motion is $\langle \alpha^2 \rangle = k_B T / (m_{eff} Q^2)$. It can be shown analytically that the factor $1 / (m_{eff} L_{OM}^2)$ uniquely determines the transduction of the Brownian motion for these sideband-resolved optomechanical oscillations (see Supplementary Information). To the right of each measured spectrum is the experimentally extracted mechanical frequency and value of $1 / (m_{eff} L_{OM}^2)$ (red), together with the values of these quantities obtained from equation (1) and the FEM model (blue). A good correspondence, in both frequency and transduced signal amplitude, is found across all optical and mechanical mode pairs. To achieve this level of correspondence, imperfections in the fabricated structure are taken into account by extracting the geometry from high-resolution scanning electron microscope images of the device and calculating the modified optical and mechanical modes (Fig. 3d). The resulting measured value for optomechanical

e–g, Zoomed r.f. mechanical spectra of Device 1 showing pinch (red), accordion (green) and breathing (blue) modes. **h**, r.f. spectra of the fundamental breathing mode (from a third device) at low (15 μW) and high (190 μW) coupled optical power. At high optical power the breathing mode is optically amplified through dynamical back-action of the radiation pressure force, with an above-threshold effective Q -factor greater than 10^6 .

coupling between the fundamental breathing and optical mode (assuming a FEM-calculated motional mass of $m_{eff} = 330$ fg) is $L_{OM} = 2.9$ μm, approaching the limit of half the effective in-material wavelength of light. The sensitivity of the mechanical transduction of the fundamental breathing mode can be appreciated by comparing the mode's r.m.s. thermal amplitude at $T = 300$ K, $\alpha_{thermal} = 245$ fm, to its quantum zero-point motion of $\alpha_{zero-point} = 3.2$ fm. The sensitivity limit, as given by the background level in the middle panel of Fig. 3c, is thus a factor of ~ 7.5 times that of the standard quantum limit.

The loss of mechanical energy from the confined mechanical modes of a phononic crystal can, in principle, be made arbitrarily low (and thus the mechanical Q arbitrarily high) by including a large number of unit cells outside the localizing defect region. Of course, other forms of mechanical damping, such as thermo-elastic damping, phonon–phonon scattering, or surface damping effects, would eventually become dominant²³. For the fundamental breathing mode of the one-dimensional phononic crystal structures studied here, we measured an intrinsic mechanical Q -factor as high as 2,700 in air, at room temperature, and in contact with the taper waveguide (see the sub-threshold spectrum of Fig. 2h). This corresponds to a frequency- Q product of $\sim 6 \times 10^{12}$ Hz, a value close to the largest yet shown²⁴. Although further tests (as a function of lattice periods, temperature, material processing, and so on) are required to determine the contribution of various mechanical loss mechanisms, numerical simulations show that mode coupling between localized and leaky phonon modes exist in these one-dimensional cavity structures and can significantly limit the Q -factor (Supplementary Information). This obstacle can be overcome in two-dimensional periodic slab structures, which have been shown to possess complete gaps for both optical and mechanical modes simultaneously²⁵, indicating that optomechanical crystals may be used to probe sensitively the fundamental loss mechanisms within nanomechanical systems.

The experimental demonstration of optomechanical coupling between 200 THz photons and 2 GHz phonons in a planar optomechanical crystal points to new methods of probing, stimulating and

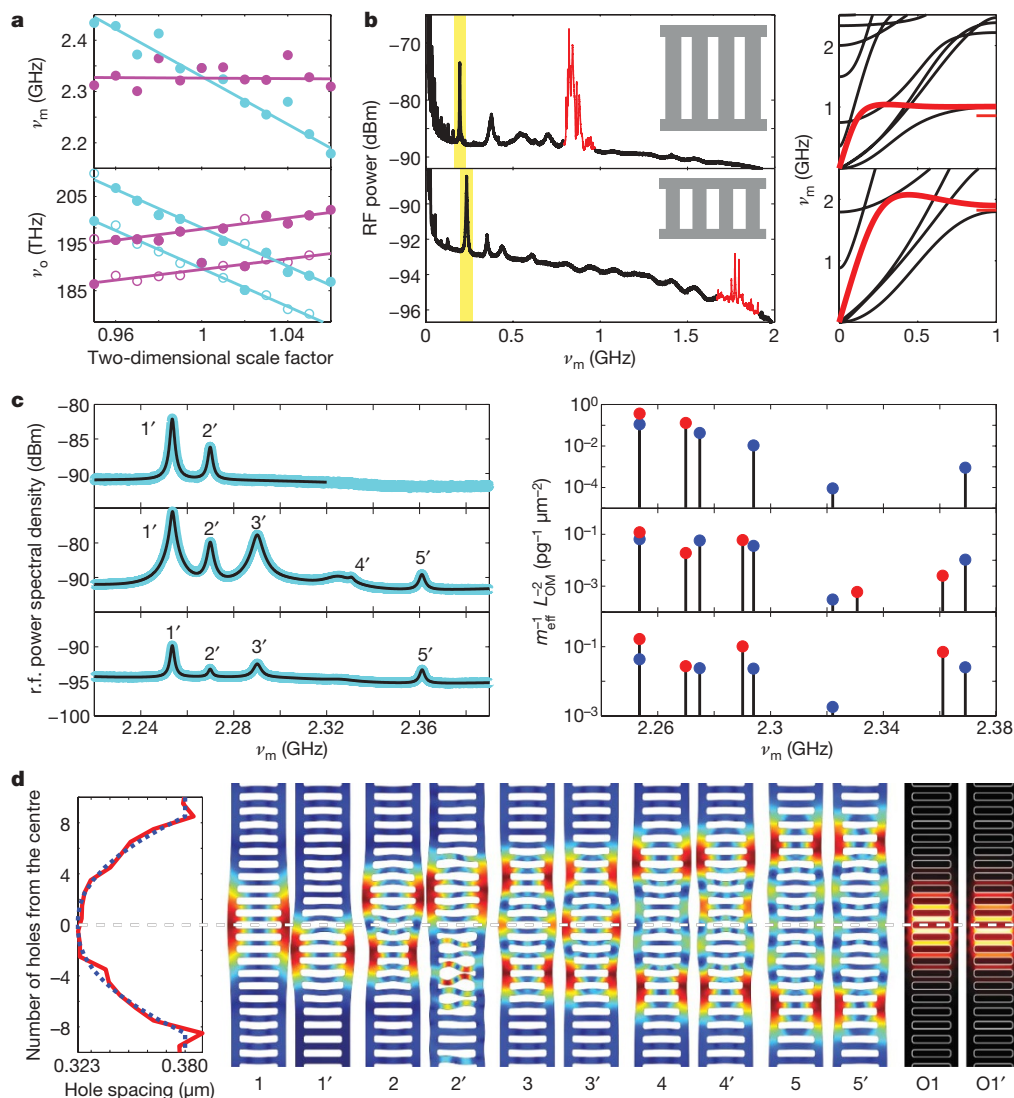


Figure 3 | Phononic mode tuning and transduction. **a**, Geometric scaling (planar) of the fundamental breathing mode. The frequencies plotted in magenta are the normalized frequencies, that is, the bare frequencies (cyan) times the scale factor for the device. The top panel shows the fundamental mechanical mode frequency, and the bottom panel shows the two lowest-order optical cavity mode frequencies. Device 1 is the device with scale factor 1.03. The best linear least-squares fit lines in the top panel correspond to a mechanical frequency change of $-0.9\% \pm 0.2\%$ per device; the normalized mechanical frequency changes by $-0.01\% \pm 0.2\%$ per device. The optical frequency of the mode used to make the mechanical measurement is filled (the other optical mode is open). **b**, Engineering of pinch mode frequencies, showing two devices (grey, insets) with pinch mode frequencies of 850 MHz (top) and 1.75 GHz (bottom). The mechanical band diagrams of each

using mechanical and optical interactions in a chip-scale platform. In particular, the efficient interconversion of photons and phonons enables a new class of optically powered oscillators²² (such as that shown in Fig. 2h), phonon-mediated optical delay lines, and wide-band optical frequency conversion. The ability to generate, distribute, and interconnect optical and mechanical excitations on a single microchip enables more complex functionality, such as filters and mixers for r.f./microwave photonics signal processing²⁶, non-reciprocal photonic structures for optical isolation²⁷, and dynamic routing/buffering of optical signals²⁸. The realization of optomechanical crystals in piezoelectric or light-emitting semiconductor materials such as gallium arsenide provides a further electronic interface for integration with microelectronic systems. In the rapidly developing field of mesoscopic quantum mechanical systems^{18,29}, optomechanical crystals offer a unique architecture for such studies

structure are shown to the right of the measured r.f. spectrum, with the pinch mode band highlighted in red. **c**, Transduction of breathing mode motion. Left panels, measured r.f. spectrum of the optical transmission intensity for the first three optical modes (top to bottom panels), with breathing modes labelled from the fundamental mode (1') to the fifth order mode (5'). Right panels, corresponding measured (red) and modelled (blue) transduction amplitude and frequency of the breathing modes. See text and Supplementary Information for details. **d**, FEM-simulated ideal (unprimed) and actual (primed) breathing modes of the silicon nanobeam cavity due to the ideal (blue dashed curve) and actual (red solid curve) lattice pitch in the defect region of the cavity. The first five mechanical modes are shown, along with the fundamental optical mode 'O1'.

with their high frequency of operation and phononic bandgap shielding from the thermal bath. Finally, optomechanical crystals could also be used as high-spatial-resolution mass sensors: with $m_{\text{eff}} = 62$ fg and $\nu_m = 850$ MHz, the mass of a single haemoglobin A protein ($\sim 10^{-19}$ g) would change the frequency of the pinch mode by 700 Hz, allowing a sensitivity similar to that of nano electro-mechanical systems zeptogram mass sensors³⁰.

METHODS SUMMARY

The optomechanical crystal nanobeam is formed in the 220-nm-thick silicon device layer of a [100] silicon-on-insulator wafer. The pattern is defined in electron beam resist by electron beam lithography. The resist pattern is transferred to the device layer by an inductively coupled plasma reactive ion etch with a $\text{C}_4\text{F}_8/\text{SF}_6$ gas chemistry. The nanobeam is then undercut and released from the silica BOX (buried oxide) layer by wet undercutting with hydrofluoric acid.

The experimental set-up used to measure the optical, mechanical and optomechanical properties of the silicon optomechanical crystal consists of a bank of fibre-coupled tunable infrared lasers spanning approximately $\Delta\lambda = 200$ nm in wavelength, centred around $\lambda = 1,520$ nm. After passing through a variable optical attenuator and fibre polarization controller, light enters the tapered and dimpled optical fibre, the position of which can be controlled with nanometre-scale precision. The transmission from the fibre is (optionally) passed through another variable optical attenuator and finally reaches an avalanche photodiode with a transimpedance gain of 1.1×10^4 and a bandwidth (3 dB rolloff point) of 1.2 GHz. The avalanche photodiode has an internal bias tee, and the r.f. voltage is connected to the 50-ohm input impedance of a high-speed oscilloscope. The oscilloscope can perform a Fourier transform to yield the r.f. power spectral density, which is calibrated using a frequency generator that outputs a variable-frequency sinusoid with known power.

Received 5 June; accepted 23 September 2009.

Published online 18 October 2009.

- Yablonovitch, E. Inhibited spontaneous emission in solid-state physics and electronics. *Phys. Rev. Lett.* **58**, 2059–2062 (1987).
- Cregan, R. F. *et al.* Single-mode photonic band gap guidance of light in air. *Science* **285**, 1537–1539 (1999).
- Notomi, M. *et al.* Extremely large group-velocity dispersion of line-defect waveguides in photonic crystal slabs. *Phys. Rev. Lett.* **87**, 253902 (2001).
- Akahan, Y., Asano, T., Song, B.-S. & Noda, S. Fine-tuned high-q photonic-crystal nanocavity. *Opt. Express* **13**, 1202–1214 (2005).
- Soljačić, M. *et al.* Photonic-crystal slow-light enhancement of nonlinear phase sensitivity. *J. Opt. Soc. Am. B* **19**, 2052–2059 (2002).
- McNab, S. J., Moll, N. & Vlasov, Y. A. Ultra-low loss photonic integrated circuit with membrane-type photonic crystal waveguides. *Opt. Express* **11**, 2927–2939 (2003).
- Olsson, R. H. III & El-Kady, I. Microfabricated phononic crystal devices and applications. *Meas. Sci. Technol.* **20**, 012002, 1–13 (2009).
- Kushwaha, M. S., Halevi, P., Dobrzynski, L. & Djafari-Rouhani, B. Acoustic band structure of periodic elastic composites. *Phys. Rev. Lett.* **71**, 2022–2025 (1993).
- Montero de Espinosa, F. R., Jiménez, E. & Torres, M. Ultrasonic band gap in a periodic two-dimensional composite. *Phys. Rev. Lett.* **80**, 1208–1211 (1998).
- Sánchez-Pérez, J. V. *et al.* Sound attenuation by a two-dimensional array of rigid cylinders. *Phys. Rev. Lett.* **80**, 5325–5328 (1998).
- Robertson, W. M. & Rudy, J. F. III. Measurement of acoustic stop bands in two-dimensional periodic scattering arrays. *J. Acoust. Soc. Am.* **104**, 694–699 (1998).
- Olsson, R. H. III, El-Kady, I. F., Su, M. F., Tuck, M. R. & Fleming, J. G. Microfabricated vhf acoustic crystals and waveguides. *Sens. Actuators A* **145–146**, 87–93 (2008).
- Khelif, A., Djafari-Rouhani, B., Vasseur, J. O. & Deymier, P. A. Transmission and dispersion relations of perfect and defect-containing waveguide structures in phononic band gap materials. *Phys. Rev. B* **68**, 024302 (2003).
- Trigo, M., Bruchhausen, A., Fainstein, A., Jusserand, B. & Thierry-Mieg, V. Confinement of acoustical vibrations in a semiconductor planar phonon cavity. *Phys. Rev. Lett.* **89**, 227402 (2002).
- Kang, M. S., Nazarkin, A., Brenn, A. & Russell, P. S. J. Tightly trapped acoustic phonons in photonic crystal fibres as highly nonlinear artificial raman oscillators. *Nature Phys.* **5**, 276–280 (2009).
- Maldovan, M. & Thomas, E. L. Simultaneous localization of photons and phonons in two-dimensional periodic structures. *Appl. Phys. Lett.* **88**, 251907 (2006).
- Chan, J., Eichenfield, M., Camacho, R. & Painter, O. Optical and mechanical design of a “zipper” photonic crystal optomechanical cavity. *Opt. Express* **17**, 3802–3817 (2009).
- Kippenberg, T. J. & Vahala, K. J. Cavity optomechanics: back-action at the mesoscale. *Science* **321**, 1172–1176 (2008).
- Favero, I. & Karrai, K. Optomechanics of deformable optical cavities. *Nature Phys.* **3**, 201–205 (2009).
- Johnson, S. G. *et al.* Perturbation theory for Maxwell’s equations with shifting material boundaries. *Phys. Rev. E* **65**, 066611 (2002).
- Michael, C. P., Borselli, M., Johnson, T. J., Chrystal, C. & Painter, O. An optical fiber-taper probe for wafer-scale microphotonic device characterization. *Opt. Express* **15**, 4745–4752 (2007).
- Rokhsari, H., Kippenberg, T. J., Carmon, T. & Vahala, K. J. Radiation-pressure-driven micromechanical oscillator. *Opt. Express* **13**, 5293–5301 (2005).
- Mohanty, P. *et al.* Intrinsic dissipation in high-frequency micromechanical resonators. *Phys. Rev. B* **66**, 085416 (2002).
- Weinstein, D. & Bhawe, S. A. Internal dielectric transduction of a 4.5 ghz silicon bar resonator. *IEEE Int. Electron. Devices Meeting* 415–418 (2007).
- Maldovan, M. & Thomas, E. Simultaneous complete elastic and electromagnetic band gaps in periodic structures. *Appl. Phys. B* **83**, 595–600 (2006).
- Hosseini-Zadeh, M. & Vahala, K. J. Photonic rf down-converter based on optomechanical oscillation. *IEEE Photon. Technol. Lett.* **20**, 234–236 (2008).
- Yu, Z. & Fan, S. Complete optical isolation created by indirect interband photonic transitions. *Nature Photon.* **3**, 91–94 (2009).
- Lin, Q. *et al.* Coherent mixing of mechanical excitations in nano-optomechanical structures. Preprint at <<http://arxiv.org/abs/0908.1128>> (2009).
- Schwab, K. C. & Roukes, M. L. Putting mechanics into quantum mechanics. *Phys. Today* **58**, 36–42 (2005).
- Yang, Y. T., Callegari, C., Feng, X. L., Ekinci, K. L. & Roukes, M. L. Zeptogram-scale nanomechanical mass sensing. *Nano Lett.* **6**, 583–586 (2006).

Supplementary Information is linked to the online version of the paper at www.nature.com/nature.

Acknowledgements Funding for this work was provided by a DARPA seed grant (grant no. HR0011-08-0002) and the National Science Foundation (EMT grant no. 0622246, MRSEC grant no. DMR-0520565, and CIAN grant no. EEC-0812072 through University of Arizona).

Author Contributions M.E., J.C., and R.C. performed the design, fabrication, and testing of devices. M.E., K.J.V., and O.P. developed the device concept and planned the measurements. All authors worked together to write the manuscript.

Author Information Reprints and permissions information is available at www.nature.com/reprints. Correspondence and requests for materials should be addressed to O.P. (opainter@caltech.edu).